

Double-site Substitution of Ce into (Ba, Sr)MnO₃ Perovskites for Solar Thermochemical Hydrogen Production

Su Jeong Heo^{1*}, Michael Sanders², Ryan O'Hayre², and Andriy Zakutayev^{1*}

¹Materials Science Center, National Renewable Energy Laboratory, Golden, CO 80401 USA

²Metallurgical and Materials Engineering, Colorado School of Mines, Golden, CO 80401 USA

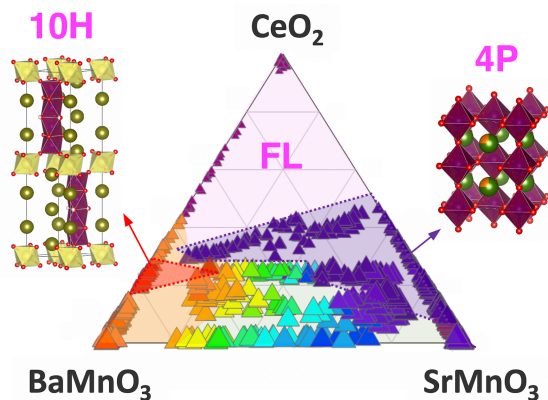
Corresponding Author

*Su Jeong Heo: SuJeong.Heo@nrel.gov, Andriy Zakutayev: Andriy.Zakutayev@nrel.gov

ABSTRACT

Solar thermochemical hydrogen production (STCH) is a renewable alternative to hydrogen produced using fossil fuels. While serial bulk experimental methods can accurately measure STCH performance, screening chemically complex materials systems for new promising candidates is more challenging. Here we identify double-site Ce-substituted (Ba,Sr)MnO₃ oxide perovskites as promising STCH candidates using a combination of bulk synthesis and high-throughput thin film experiments. The Ce substitution on the B-site in 10H-BaMnO₃ and on the A-site in 4P-SrMnO₃ lead to 2-3x higher hydrogen production compared to CeO₂, but these bulk single-site substituted perovskites suffer from incomplete reoxidation. Double-site Ce substitution on both A- and B-site in (Ba,Sr)MnO₃ thin films increases Ce solubility and extends the stability of 10H and 4P structures, which is promising for their thermochemical reversibility. This study demonstrates a high-throughput experimental method for screening complex oxide materials for STCH applications.

TOC GRAPHICS



Hydrogen is a valuable chemical precursor and storable energy carrier that is widely used in ammonia production and fuel cell vehicles.^{1,2} Hydrogen produced by water electrolysis using renewable electricity is a sustainable alternative to steam reforming of natural gas.³⁻⁷ Among several emerging hydrogen production routes (e.g., photoelectrochemical, electrolysis), solar thermochemical hydrogen production (STCH) has received considerable attention.⁸⁻¹⁰ One of the possible STCH cycles is a two-step water-splitting process, involving partial thermal reduction of a suitable metal oxide, followed by steam based reoxidation for hydrogen production. Non-stoichiometric pure and doped ceria (CeO_2) compounds have been widely investigated for this STCH process.¹¹⁻¹³ However, the low extent of ceria reduction required hydrogen production under very high temperatures ($>1500\text{ }^\circ\text{C}$), increasing the difficulty of engineering suitable reactors.¹⁴

Oxide materials with perovskite and perovskite-related structures are promising alternative redox candidates for replacing ceria in STCH applications.^{15,16} The ABO_3 perovskite composition can accommodate a variety of A- and B-site cations and structure variations, enabling broad opportunities to control the extent of oxygen reduction.^{17,18} Perovskite oxides tend to easily form point defects such as oxygen vacancies, which facilitates fast redox reaction kinetics due to higher oxygen exchange capacities, and can also enable an increased extent of reduction at lower temperatures.¹⁹ Among currently known redox-active perovskites, $\text{BaCe}_{0.25}\text{Mn}_{0.75}\text{O}_{3-\delta}$ (BCM25)²⁰, $\text{SrTi}_{0.5}\text{Mn}_{0.5}\text{O}_{3-\delta}$ (STM55)²¹, $\text{LaGa}_{0.4}\text{Co}_{0.6}\text{O}_{3-\delta}$ (LGC60)²², $\text{La}_{1-x}\text{Sr}_x\text{MnO}_3$ (LSM)^{23,24}, and $\text{Sr}_x\text{La}_{1-x}\text{Mn}_y\text{Al}_{1-y}\text{O}_{3-\delta}$ (SLMA)²⁵ have shown particular promise for STCH application.

The staggering number of oxide perovskites compositions motivates the need for high-throughput research methods to discover the most promising perovskites for STCH application, and probe composition-structure-property relations that can improve understanding of the STCH

process. Numerous studies have sought new STCH perovskites using high-throughput computational methods.^{26,27} However, experimental (combinatorial) high-throughput method have been less explored for perovskites in STCH compared to other applications (e.g., piezoelectrics²⁸). In addition to the combinatorial screening for STCH application studied here, the oxide perovskite crystal structure and redox properties show great promise for a wide range of other applications including fuel cells,²⁹ catalysis,³⁰ and electrochemical water splitting.³¹

Here, we investigate double-site Ce substitution of (Ba,Sr)MnO₃ perovskites for solar thermochemical hydrogen production using a combination of serial bulk synthesis and high-throughput thin film methods. Temperature programmed reduction and water splitting experiments with single-site Ce substituted 10H-BaMnO₃ and 4P-SrMnO₃ bulk powder samples, suggest that double-site Ce substitution of (Ba,Sr)MnO₃ may increase Ce incorporation and improve the redox stability of these materials for STCH applications. Guided by a Goldschmidt tolerance factor model, thin film combinatorial experiments with double-site substituted (Ba,Sr)_{1-x}Ce_xCe_yMn_{1-y}O₃ are used to evaluate composition-structure-processing trends in this complex 4-cation chemical space. We find that co-doping Ce on both A-site and B-site in (Ba,Sr)MnO₃ increases overall Ce solubility and increases composition stability range of 10H and 4P structures, both of which should lead to higher STCH performance. This study provides new understanding of composition-structure-processing-property relations in the (Ba,Sr,Ce)(Mn,Ce)O₃ material system, and demonstrates an efficient way to uncover new STCH-active compounds using high-throughput experimental methods.

Bulk powders

Single-site Ce-substituted BaMnO₃ and SrMnO₃ oxide perovskites were synthesized as bulk powders, including BaCe_{0.25}Mn_{0.75}O_{3- δ} (BCM25) and Sr_{0.75}Ce_{0.25}MnO_{3- δ} (SCM25) using a sol-gel modified Pechini method³² (see supporting information for experimental details). The resulting crystal structures and the relative phase fractions were determined from X-ray diffraction (XRD) measurements and Rietveld refinement, as shown in Figure 1a. This quantification procedure revealed that the SCM25 bulk powder has almost phase-pure 4P structure (99.0%) while the BCM25 bulk powder is predominantly 10H polymorph with 7% of 12R and 7% of fluorite (FL) secondary phases. This 10H polymorph of BCM25 is likely to convert to the 12R polymorph after several redox cycles as shown in prior investigations.²⁰

The redox potential of these bulk compositions was compared using temperature-programmed reduction (TPR), with results presented in Figure 1b. The behavior of the single-site substituted BCM25 and SCM25 are compared to SrMnO₃ (SMO) simple perovskite and ceria (CeO₂), which is the current benchmark materials for STCH. While undoped ceria has a too low extent of reduction ($\Delta\delta < 0.03$) but fully reoxidizes, undoped SMO has exceptionally large extents of reduction but the driving force for reoxidation is probably too low to split water. Ce-doped BaMnO₃ and SrMnO₃ starts to reduce at considerably lower temperature (< 950 °C), with large extents of reduction ($\Delta\delta > 0.17$ for BCM25 and $\Delta\delta > 0.26$ for SCM25) compared to ceria which is beneficial for STCH. However, both BCM25 and SCM25 do not fully reoxidize ($\Delta\delta > 0.01$) compared to ceria, which is a disadvantage for STCH applications.

Water-splitting hydrogen production of single-site substituted BCM25 and SCM25 perovskites was measured under two reduction/oxidation condition sets using a stagnation flow reactor (SFR) that has been described elsewhere.³³ The results are compared to undoped ceria

baseline material and double-site substituted SLMA perovskites measured at the same conditions,²⁰ as shown in Figure 1c. BCM25 releases a larger amount of H₂ at T_{RE} 1350 °C and T_{OX} 850°C than SCM25, and SCM25 produces a larger amount of hydrogen at T_{RE} 1400°C and T_{OX} 1050 °C than BCM25.

The amounts of H₂ produced by both BCM25 and SCM25 perovskite compounds are 2-3x larger than by undoped ceria. However, the H₂ production of these single-site substituted perovskites is lower than double-site La and Al co-substituted SrMnO₃ (SLMA), which is one of the most promising perovskites for STCH.^{34,35} Similarly to double-site substitution in SLMA, the STCH performance in Ba_{1-x}Sr_xCo_yFe_{1-y}O_{3.δ}³⁶ and Ca_{0.5}Ce_{0.5}MO₃ (M = 3d transition metals)³⁷ material systems has been suggested and demonstrated to increase STCH performance. Thus, it is likely that similar improvements of STCH performance should be possible in the double site substituted (Ba,Sr)_{1-x}Ce_xCe_yMn_{1-y}O₃ perovskite in the compositional stability range at high temperature.

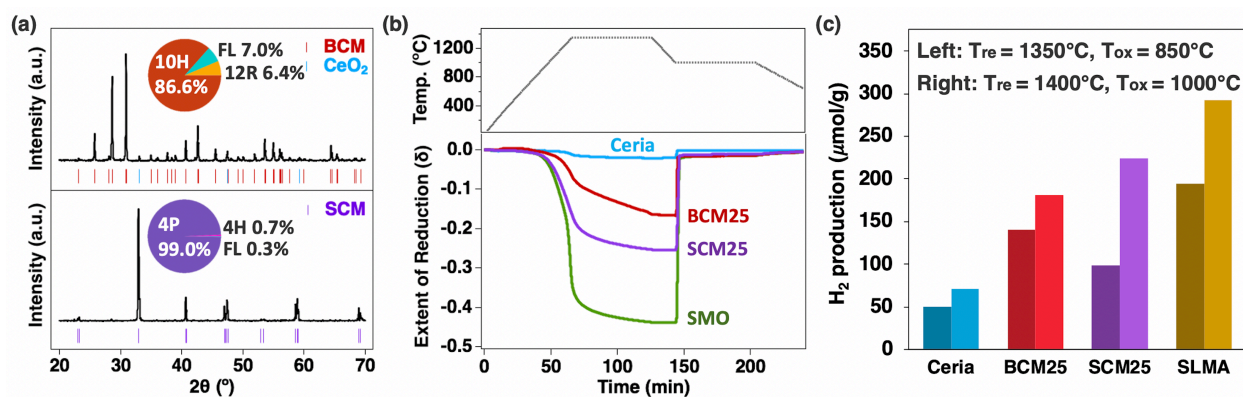


Figure 1. Characterization of STCH-active perovskites and ceria in bulk powder form: (a) XRD and Rietveld refinement for the BCM25 and SCM25 powders used as end-member targets, (b) Temperature Programmed Reduction for single-site substituted BCM25 and SCM25 and undoped CeO₂ and BaMnO₃

bulk samples, and (c) STCH performance of SCM25 powders and other compounds reported elsewhere²⁰ for the conditions of $T_{\text{red}}=1350^{\circ}\text{C}$ & $T_{\text{ox}}=850^{\circ}\text{C}$ and $T_{\text{red}}=1400^{\circ}\text{C}$ & $T_{\text{ox}}=1000^{\circ}$.

Substitution model

To predict the structural trends in the (Ba,Sr,Ce)(Ce,Mn)O₃ perovskite materials system studied here, we use the Goldschmidt tolerance factor. The Goldschmidt tolerance factor³⁸ reflects the degree of the ideal cubic perovskite distortion that can arise from a size-mismatch of cations and anions, defined as $t = \frac{r_A+r_O}{\sqrt{2}(r_B+r_O)}$ where r_A , r_B , and r_O represent the average ionic radii of the A, B, and O-sites, respectively. Generally, cubic symmetry with minor distortion of the corner-sharing BO₆ octahedra is found for compounds where the tolerance factor lies between roughly 0.9 and 1.0. As the value of t increases above 1, the ratio of face-sharing to corner-sharing octahedra increases to accommodate the correspondingly larger A-site cations and/or smaller B-site cations which can lead to the formation of hexagonal structures.

Figure 2 illustrates the modeled changes in tolerance factor within the (Ba,Sr,Ce)(Ce,Mn)O₃ chemical composition quaternary (Fig. 2a) and pseudo-ternary (Fig. 2b) phase diagrams containing the BaMn_{1-y}Ce_yO₃ (BCM), Sr_{1-x}Ce_xMnO₃ (SCM), Ba_{1-x}Sr_xMnO₃ (BSM), and (Ba,Sr)_{1-x}Ce_xMn_{1-y}Ce_yO₃ (BSCMC) compositional families of interest to this study. The BaMnO₃ has a calculated Goldschmidt tolerance factor (t) of 1.103 which is far greater than unity, so BaMnO₃ forms a hexagonal 2H structure.³⁹ With the B-site substitution of smaller Mn ions by larger Ce ions in BaMnO₃, the 1.103 tolerance factor gradually decreases and reaches 1.056 at 25% Ce incorporation in Ba(Ce,Mn)O₃ resulting in the 10H structure⁴⁰ (BCM25). The tolerance factor of BaMnO₃ is also reduced with A-site substitution of smaller Ba ions by smaller Sr ions along the BaMnO₃/SrMnO₃ tie-line, ending with $t = 1.041$ for pure strontium manganate's 4H structure.⁴¹

To further decrease the tolerance factor, it is possible to reduce some of the Mn^{4+} to Mn^{3+} by partially substituting the Sr^{2+} by Ce^{3+} on A-site of SrMnO_3 while keeping the charge balance for stability. In this case, the simultaneous increase of the B-site and decrease of the A-site mean ionic radii lead to rapid lowering of the tolerance factor, reaching 0.993 for $\text{Sr}_{0.5}\text{Ce}_{0.5}\text{MnO}_3$, which shows a tetragonal-like perovskite structure ($I4/mcm$).⁴² The tolerance factor can be also lowered by increasing the compositional complexity of the material with simultaneous A and B-site doping. As shown in Figure 2, starting from BCM25, the tolerance factor is gradually decreased by substituting Sr on A-site while it more steeply decreases by substituting both Sr and Ce in $(\text{Ba,Sr})(\text{Ce,Mn})\text{O}_3$. Finally, combining all of these effects, the $(\text{Ba,Sr,Ce})(\text{Ce,Mn})\text{O}_3$ compositions is of interest in this study to achieve smaller tolerance factors by moving from BCM25 towards higher concentrations of Sr and Ce.

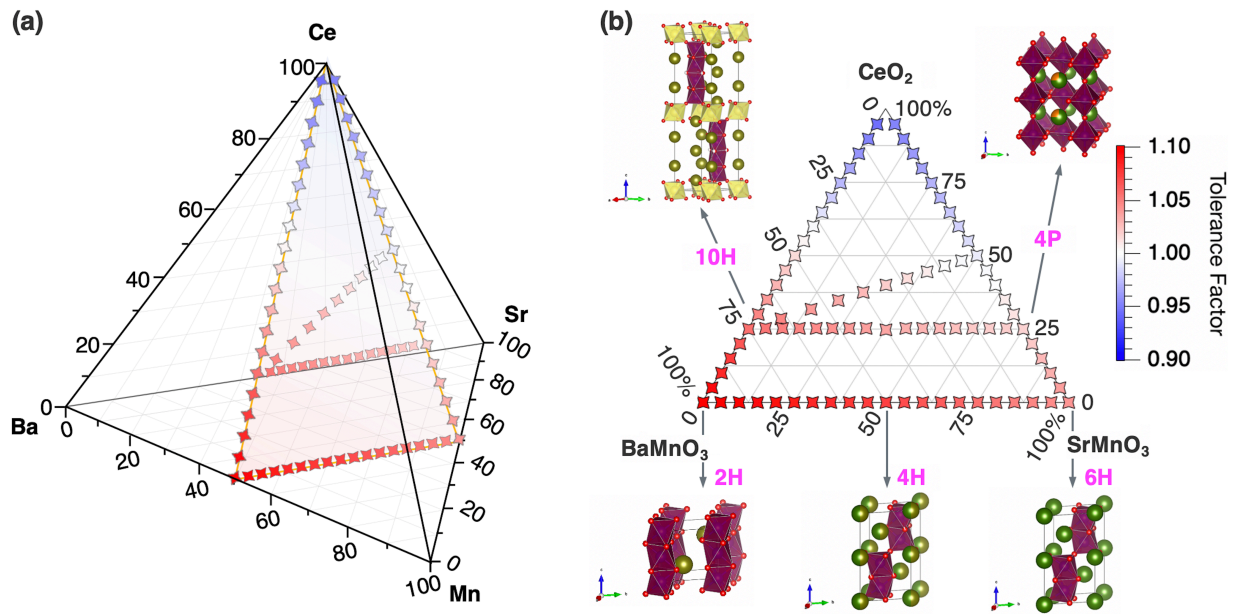


Figure 2. Model of single- and double-site Ce substitution into $(\text{Ba,Sr})\text{MnO}_3$ perovskites: (a) Goldschmidt tolerance factor over the composition space of the BSCM quaternary phase diagram and (b) BaMnO_3 - SrMnO_3 - CeO_2 ternary phase diagram with corresponding crystal structures. Single- and double-site Ce

substitution of (Ba,Sr)MnO₃ may induce a structural change due to reductions in the tolerance factor. CeO₂ has a fluorite structure (FL), so the perovskite tolerance factor values have decreasing significance as the compositions shift towards pure ceria.

Single site substitution

To validate the predictions of our (Ba,Sr,Ce)(Ce,Mn)O₃ structural model (Fig. 2), we used combinatorial pulsed laser deposition (PLD) to synthesize sample libraries with many chemical compositions (Figure 3),⁴³ and anneal them at elevated temperature in air. These sample libraries are evaluated for their composition, structure and properties using spatially-resolved measurement techniques (see supporting information for experimental details). Figure 3a shows the pseudo-ternary phase diagrams of the structure of BaCe_yMn_{1-y}O₃, Sr_{1-x}Ce_xMnO₃, and Ba_{1-x}Sr_xMnO₃ pseudo-binary tie-lines along its edges. The structures of these perovskite-related oxides can be distinguished by X-ray diffraction in the range of $2\theta = 30.7\text{-}33.2^\circ$ based on small peak shifts (Figure 3b). For example, in the case of BaMnO₃ in Figure 3a, a two-layer hexagonal (2H) structure featuring face-shared oxygen polyhedron with a space group of $P6_3/mmc$,³⁹ has been determined from its signature XRD peak at 31.4 degrees.

As shown in Figure 3a, the 2H-BaMnO₃ B-site substitution of Mn⁴⁺ by Ce⁴⁺ or Ce³⁺ along the BaCe_yMn_{1-y}O₃ tie-line leads to the formation of a 10H-BaCe_{0.25}Mn_{0.75}O₃ (10H-BCM25) structure reported to be promising for STCH²⁰, which is formed via face-sharing octahedral [Mn₄O₁₅] tetramers that share corners with [Ce_{0.83}Mn_{0.17}O₆] octahedral along the *c*-axis.⁴⁰ The 2H-BaMnO₃ A-site replacement of larger Ba²⁺ ($r = 1.61 \text{ \AA}$ in 12-fold coordination) with smaller Sr²⁺ ($r = 1.44 \text{ \AA}$ in 12-fold coordination) leads to the 4H-polymorph of SrMnO₃ (Figure 3a), which contains both corner- and face-sharing octahedra.⁴⁴⁻⁴⁶ In between BaMnO₃ and SrMnO₃, the Sr_xBa_{1-x}MnO₃ alloy,

with the varying oxygen stoichiometry determined by the ratio of corner-sharing (cubic) to face-sharing (hexagonal) octahedra, may offer additional STCH candidates with tailored oxygen vacancy formation energies. Substituting the A-site Sr^{2+} in 4H-SrMnO_3 with smaller Ce^{3+} ($r = 1.34 \text{ \AA}$, CN=12) and/or Ce^{4+} ($r = 1.14 \text{ \AA}$, CN=12) leads to a structural phase transition from 4H hexagonal symmetry ($P6_3/mmc$) to 4P tetragonal-like symmetry ($I4/mcm$).⁴⁷

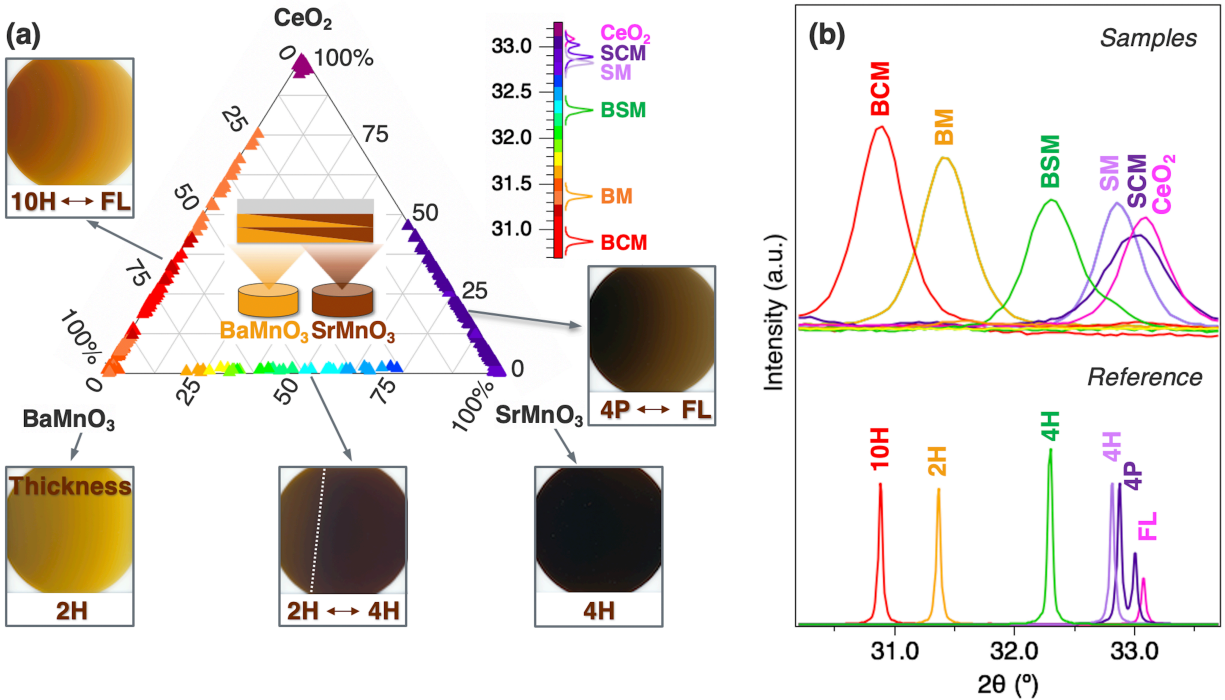


Figure 3. The $(\text{Ba,Sr,Ce})(\text{Ce,Mn})\text{O}_3$ thin-film pseudo-ternary phase diagram: (a) XRD 2θ position of the primary peaks mapped over the composition space of the BaMnO_3 - SrMnO_3 - CeO_2 ternary phase diagram with corresponding film images. (b) Representative sample XRD patterns of the primary peaks of each sample and reference patterns for comparison. The individual structures in this complicated phase space can be distinguished by XRD in the range of $2\theta = 30.7\text{-}33.2^\circ$.

In addition to XRD, the color has been measured for the compositionally graded thin films annealed at $950 \text{ }^\circ\text{C}$ (Fig. 3a) using an optical scanner,⁴⁸ which is an important metric because it potentially can be used to evaluate the extent of reduction in thermochemical cycling. The pale-

green color of 2H-BaMnO₃ thin films is consistent with the dark-green color of bulk powder.³⁹ As Ce is substituted on B-site of 2H-BaMnO₃, the film color changes to bright-orange when it forms the 10H structure at the BCM25 composition, and changes to a light-yellow color at higher Ce-fractions. The dark-brown color of 4H-SrMnO₃ is in good agreement with a bulk powder report,⁴⁹ and also lightens as Ce is substituted on A-site of 4H-SrMnO₃ to form the 4P structure of SCM25 with inclusions of FL at yet-higher Ce fraction. As the annealing temperature increases above 950 °C, the overall film colors became darker, followed by separation on black and white as expected from segregation of the CeO₂ fluorite (FL) secondary phases.

Double site substitution

Now that the site substitution model for (Ba,Sr)_{1-x}Ce_xCe_yMn_{1-y}O₃ has been established (Fig. 2) and validated (Fig. 3), we explore the potential to further increase the Ce concentration in the oxide perovskite materials by substituting the A-site with Ba in (Sr,Ce)MnO₃ and with Sr in Ba(Ce,Mn)O₃, which should enhance the stability of the perovskite structure and lead to improved STCH performance. The pseudo-ternary (Ba,Sr)_{1-x}Ce_xCe_yMn_{1-y}O₃ phase diagram in Figure 4 shows the dominant structure determined from XRD 2θ position (color scale map) and relative perovskite phase intensity-ratio (marker size) within the BaMnO₃-SrMnO₃-CeO₂ phase space after annealing at elevated temperatures.

Along the BaMnO₃-CeO₂ tie line in Figure 4a, the 10H structure is observed in a wide Ce-concentration range (about 13-42%) at 950 °C, but with low perovskite phase ratio above 25% Ce. When Sr is incorporated in Ba(Ce,Mn)O₃, the 10H structure region increases to higher Ce concentration (~32%) with higher perovskite phase ratio. Since BCM is reported to form a line compound with an exact Ce/Mn ratio of 0.25/0.75 due to size constraints on the B-site⁵⁰, this result

shows that excess Ce above 25% may be accommodated by substitution on the A-site. With increasing temperature, the Sr-free 10H structure (red color in Fig. 4) diminishes and eventually disappears at 1150 °C (in Fig. 4c). However, the Sr-containing 10H structure transitions to the 4P structure in this high temperature range. This suggests that Sr-substituted $\text{Ba}(\text{Ce},\text{Mn})\text{O}_3$ with 4P structure is a new promising candidate for STCH applications, in accordance with our double site substitution model (Figure 2)

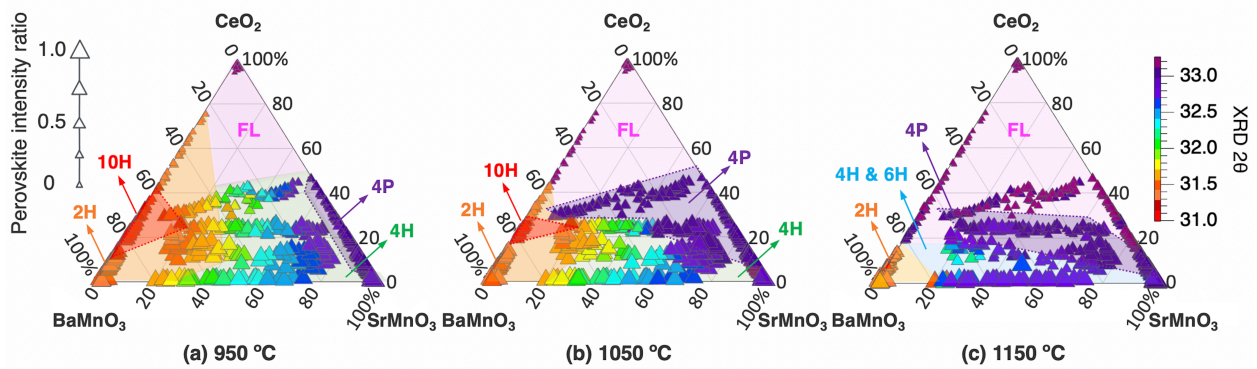


Figure 4. Double-site Ce substitution into thin-film $(\text{Ba},\text{Sr})\text{MnO}_3$ perovskites, showing XRD 2θ position (color scale map) and perovskite phases-ratio (marker size) measured over the composition space of BM-SM-Ce oxide ternary phase diagram after 950 °C (a), 1050 °C (b), and 1150 °C (c) annealing in air. Double site Ce substitution into $(\text{Ba},\text{Sr})\text{MnO}_3$ increases the composition range of stability for 10H and 4P structures suitable for STCH as illustrated for bulk powders in Fig.1.

Along the SrMnO_3 - CeO_2 tie line in Figure 4, the 4P structure appears when Ce is substituted in $(\text{Sr},\text{Ce})\text{MnO}_3$ and persists up to 55% Ce-concentration at 950 °C (Fig. 4a) and 1050 °C (Fig. 4b), while the perovskite-ratio decreases at higher Ce-concentration and at the highest temperature of 1150 °C (Fig. 4c). As discussed above, the 4P structure can accommodate very high Ba concentration (max. $\sim 92\%$ at 1050 °C) into $(\text{Sr}, \text{Ce})\text{MnO}_3$ which can be observed in the center area of the phase diagram in Figure 4. Although the 4P structure coexists with FL structure, the

FL-ratio decreases upon Ba-doping at the same Ce-concentration line (horizontal lines in Fig. 4), implying that the Ba substitution permits additional Ce to be accommodated into the 4P structure. Again, this suggests that Ba-substituted (Sr,Ce)MnO₃ with 4P structure may be promising for STCH applications due to a broader compositional range of stability and its ability to accommodate higher Ce content compared to BCM.

Conclusions

In summary, the screening of the (Ba, Sr, Ce)(Mn, Ce)O₃ space by a combination of serial bulk synthesis and high-throughput thin film experimentations indicates that the composition stability range of tetragonal 4P-polymorph of (Sr,Ce)MnO₃ can be significantly enhanced by up to 90% Ba-substitution even at temperatures >1000 °C. In addition, the compositional stability range of the hexagonal 10H-polymorph is enhanced by substitution of Sr into Ba(Ce,Mn)O₃, while the total Ce fraction is increased, and a FL secondary phase content is reduced. These thin film results are supported by bulk powder measurement of high thermochemical water splitting performance of these 4P (e.g. SCM25) and 10H (e.g. BCM25) which is 2-3x larger compared to the ceria baseline material. Our work not only demonstrates an experimental high-throughput approach to identify new redox materials for renewable hydrogen production, but also provides general insights into composition-structure-property relations for designing oxide perovskites by double site substitution for other energy applications.

ASSOCIATED CONTENT

Supporting Information. Bulk experimental methods, including powder synthesis and their XRD, Rietveld refinement, TPR characterization, and water splitting measurements. Thin film experimental methods including combinatorial deposition of single- and double-site substituted perovskite by PLD system with post annealing, spatially-resolved XRD and XRF for mapping of the perovskite films.

AUTHOR INFORMATION

Corresponding Authors

Su Jeong Heo - Materials Science Center, National Renewable Energy Laboratory, Golden, CO 80401 USA; orcid.org/0000-0002-7933-9714; Email: SuJeong.Heo@nrel.gov

Andriy Zakutayev - Materials Science Center, National Renewable Energy Laboratory, Golden, CO 80401 USA; orcid.org/0000-0002-3054-5525; Email: Andriy.Zakutayev@nrel.gov

Authors

Michael Sanders - Metallurgical and Materials Engineering, Colorado School of Mines, Golden, CO 80401 USA; orcid.org/0000-0001-6366-5219; Email: misander@mymail.mines.edu

Ryan O'Hayre - Metallurgical and Materials Engineering, Colorado School of Mines, Golden, CO 80401 USA; orcid.org/0000-0003-3762-3052; Email: rohayre@mines.edu

Notes

The authors declare no competing financial interest.

ACKNOWLEDGMENT

This work was authored in part by the National Renewable Energy Laboratory (NREL), operated by Alliance for Sustainable Energy LLC, for the U.S. Department of Energy (DOE) under contract no. DE-AC36-08GO28308. Funding provided by the Office of Energy Efficiency and Renewable Energy (EERE) Hydrogen and Fuel Cell Technologies Office (HFTO), as a part of HydroGEN Energy Materials Network (EMN) consortium. The authors would like to acknowledge the use of a stagnation flow reactor (SFR) at Sandia National Laboratories, which is a multimission laboratory managed and operated by National Technology and Engineering Solutions of Sandia, LLC, a wholly owned subsidiary of Honeywell International Inc., for the U.S. Department of Energy's National Nuclear Security Administration under contract DE-NA0003525. We would also like to thank Dr. Yun Xu for preliminary data and initial discussions related to this work. The views expressed in the article do not necessarily represent the views of the DOE or the U.S. Government.

REFERENCES

- 1 Ganguly, P; Harb, M; Cao, Z; Cavallo, L; Breen, A; Dervin, S; Dionysiou, D. D.; Pillai, S. C. 2D Nanomaterials for Photocatalytic Hydrogen Production. *ACS Energy Lett.* **2019**, 4, 1687-1709.
- 2 Marban, G.; Valdés-Solis, T. Towards the Hydrogen Economy? *Int. J. Hydrogen Energy* **2007**, 32, 1625-1637.
- 3 Chu, S.; Majumdar, A. Opportunities and Challenges for a Sustainable Energy Future. *Nature* **2012**, 488, 294-303.

- 4 Yan, Z.; Hitt, J. L.; Turner, J. A.; Mallouk, T. E. Renewable Electricity Storage using Electrolysis. *PNAS* **2020**, 117, 12558-12563.
- 5 Alsayegh, S. O.; Varjian, R.; Alsalik, Y.; Katsiev, K.; Isimjan, T. T.; Idriss, H. Methanol Production Using Ultrahigh Concentrated Solar Cells: Hybrid Electrolysis and CO₂ Capture. *ACS Energy Lett.* **2020**, 5, 540-544.
- 6 Gray, H. B. Powering the Planet with Solar Fuel. *Nature Chem.* **2009**, 1, 7.
- 7 Alexandratos, S. D.; Barak, N.; Bauer, D.; Davidson, F. T.; Gibney, B. R.; Hubbard, S. S.; Taft, H. L.; Westerhof, P. Sustaining Water Resources: Environmental and Economic Impact. *ACS Sustainable Chem. Eng.* **2019**, 7, 2879-2888.
- 8 Li, S.; Wheeler, V. M.; Kumar, A.; Venkataraman, M. B.; Muhich, C. L.; Hao, Y.; Lipinski, W. Thermodynamic Guiding Principles for Designing Nonstoichiometric Redox Materials for Solar Thermochemical Fuel Production: Ceria, Perovskites, and Beyond. *Energy Technol.* **2021**, 2000925.
- 9 Licht, S. Thermochemical Solar Hydrogen Generation. *Chem. Commun.* **2005**, 4635-4646.
- 10 Boettcher, S. W. Benchmarks and Protocols for Electrolytic, Photoelectrochemical, and Solar-Thermal Water-Splitting Technologies. *ACS Energy Lett.* **2020**, 5, 70-71.
- 11 Chueh, W. C.; Falter, C.; Abbott, M.; Scipio, D.; Furler, P.; Haile, S. M.; Steinfeld, A. High-Flux Solar-Driven Thermochemical Dissociation of CO₂ and H₂O Using Nonstoichiometric Ceria. *Science* **2010**, 330, 1797-1801.

- 12 Chueh, W. C.; Haile, S. M. Ceria as a Thermochemical Reaction Medium for Selectively Generating Syngas or Methane from H₂O and CO₂. *ChemSusChem*. **2009**, 2 (8), 735-739.
- 13 Riaz, A.; Ali, M. U.; Enge, T. G.; Tsuzuki T.; Lowe, A.; Lipinski, W. Concentration-Dependent Solar Thermochemical CO₂/H₂O Splitting Performance by Vanadia-Ceria Multiphase Metal Oxide Systems. *Research* **2020**, 2020, 3049534.
- 14 McDaniel, A. H. Renewable Energy Carriers Derived from Concentrating Solar Power and Nonstoichiometric Oxides. *Curr. Opin. Green Sustain. Chem.* **2017**, 4, 37-43.
- 15 Kubicek, M.; Bork, A. H.; Rupp, J. L. M. Perovskite Oxides – A Review on a Versatile Material Class for Solar-to-Fuel Conversion Processes. *J. Mater. Chem. A* **2017**, 5, 11983-12000.
- 16 Parvanian, A. M.; Salimijazi, H.; Shabaninejad, M.; Troitzsch, U.; Kreider, P.; Lipinski, W.; Saadatfar, M. Thermochemical CO₂ Splitting Performance of Perovskite Coated Porous Ceramics. *RSC Adv.* **2020**, 10, 23049.
- 17 Cooper, T.; Scheffe, J. R.; Galvez, M. E.; Jacot, R.; Patzke, G.; Steinfeld, A. Lanthanum Manganite Perovskites with Ca/Sr A-site and Al B-site Doping as Effective Oxygen Exchange Materials for Solar Thermochemical Fuel Production. *Energy Technol.* **2015**, 3, 1130-1142.
- 18 Vieten, J.; Bulfin, B.; Huck, P.; Horton, M.; Guban, D.; Zhu, L.; Lu, Y.; Persson, K. A.; Roeb, M.; Sattler, C. Materials Design of Perovskite Solid Solutions for Thermochemical Applications. *Energy Environ. Sci.* **2019**, 12, 1369-1384.

- 19 Haeussler, A.; Abanades, S.; Jouannaux, J.; Julbe, A. Non-Stoichiometric Redox Active Perovskite Materials for Solar Thermochemical Fuel Production: A Review. *Catalysts* **2018**, 8 (12), 611.
- 20 Barcellos, D. R.; Sanders, M. D.; Tong, J.; McDaniel, A. H.; O'Hayre, R. P. BaCe_{0.25}Mn_{0.75}O_{3- δ} - A Promising Perovskite-Type Oxide for Solar Thermochemical Hydrogen Production. *Energy Environ. Sci.* **2018**, 11, 3256-3265.
- 21 Qian, X.; He, J.; Mastronardo, E.; Baldassarri, B.; Wolverton, C.; Haile, S. M. Favorable Redox Thermodynamics of SrTi_{0.5}Mn_{0.5}O_{3- δ} in Solar Thermochemical Water Splitting. *Chem. Mater.* **2020**, 32, 9335-9346.
- 22 Chen, Z.; Jiang, Q.; Cheng, F.; Tong, J.; Yang, M.; Jiang, Z.; Li, C. Sr- and Co-doped LaGaO_{3- δ} with High O₂ and H₂ Yields in Solar Thermochemical Water Splitting. *J. Mater. Chem. A* **2019**, 7, 6099-6112.
- 23 Riaz, A.; Kreider, P.; Kremer, F.; Tabassum, H.; Yeoh, J. S.; Lipinski, W.; Lowe, A. Electrospun Manganese-Based Perovskites as Efficient Oxygen Exchange Redox Materials for Improved Solar Thermochemical CO₂ Splitting. *ACS Appl. Energy Mater.* **2019**, 2, 2494-2505.
- 24 Riaz, A.; Tsuzuki, T.; Kremer, F.; Sattayaporn, S.; Ali, M. U.; Lipinski, V.; Lowe, A. Structural Rearrangement in LSM Perovskites for Enhanced Syngas Production via Solar Thermochemical Redox Cycles. *ACS Catal.* **2020**, 10, 8263-8276.

- 25 Deml, A. M.; Stevanovic, V.; Holder, A. M.; Sanders, M.; O'Hayre, R.; Musgrave, C. B. Tunable Oxygen Vacancy Formation Energetics in the Complex Perovskite Oxide $\text{Sr}_x\text{La}_{1-x}\text{Mn}_y\text{Al}_{1-y}\text{O}_3$. *Chem. Mater.* **2014**, 26, 6595-6602.
- 26 Emery, A. A.; Saal, J. E.; Kirklin, S.; Hegde, V. I.; Wolverton, C. High-Throughput Computational Screening of Perovskites for Thermochemical Water Splitting Applications. *Chem. Mater.* **2016**, 28, 5621-5634.
- 27 Emery, A. A.; Wolverton, C. High-Throughput DFT Calculations of Formation Energy, Stability and Oxygen Vacancy Formation Energy of ABO_3 Perovskites. *Sci. Data* **2017**, 4, 170153.
- 28 Guerin, S.; Hayden, B. E. ABO_3 and $\text{A}_{1-x}\text{C}_x\text{B}_{1-y}\text{D}_y(\text{O}_{1-z}\text{E}_z)_3$: Review of Experimental Optimisation of Thin Film Perovskites by High-Throughput Evaporative Physical Vapour Deposition. *Chem. Commun.* **2019**, 55, 10047-10055.
- 29 He, W.; Wu, X.; Yang, G.; Shi, H.; Dong, F.; Ni, M. $\text{BaCo}_{0.7}\text{Fe}_{0.22}\text{Y}_{0.08}\text{O}_{3-\delta}$ as an Active Oxygen Reduction Electrocatalyst for Low-Temperature Solid Oxide Fuel Cells below 600 °C. *ACS Energy Lett.* **2017**, 2, 301-305.
- 30 Polo-Garzon, F.; Wu, Z. Acid-Base Catalysis over Perovskites: A Review. *J. Mater. Chem. A* **2018**, 6, 2877-2894.
- 31 Suryanto, B. H.; Wang, Y.; Hocking, R. K.; Adamson, W.; Zhao, C. Overall Electrochemical Splitting of Water at the Heterogeneous Interface of Nickel and Iron Oxide, *Nature Commun.* **2019**, 10, 5599.

- 32 Shang, M.; Tong, J.; O'Hayre, R. A Novel Wet-Chemistry Method for the Synthesis of Multicomponent Nanoparticles: A Case Study of $\text{BaCe}_{0.7}\text{Zr}_{0.1}\text{Y}_{0.1}\text{Yb}_{0.1}\text{O}_{3-\text{D}}$. *Mater. Lett.* **2013**, *92*, 382–385.
- 33 Scheffe, J. R.; Allendorf, M. D.; Coker, E. N.; Jacobs, B. W.; McDaniel, A. H.; Weimer, A. W. Hydrogen Production via Chemical Looping Redox Cycles Using Atomic Layer Deposition-Synthesized Iron Oxide and Cobalt Ferrites. *Chem. Mater.* **2011**, *23*, 2030-2038.
- 34 Ezbiri, M.; Takacs, M.; Theiler, D.; Michalsky, R.; Steinfeld, A. Tunable Thermodynamic Activity of $\text{La}_x\text{Sr}_{1-x}\text{Mn}_y\text{Al}_{1-y}\text{O}_{3-\delta}$ ($0 \leq x \leq 1, 0 \leq y \leq 1$) Perovskites for Solar Thermochemical Fuel Synthesis. *J. Mater. Chem. A* **2017**, *5*, 4172-4182.
- 35 McDaniel, A. H.; Miller, E. C.; Arifin, D.; Ambrosini, A.; Coker, E. N.; O'Hayre, R.; Chueh, W. C.; Tong, J. Sr- and Mn-doped $\text{LaAlO}_{3-\delta}$ for Solar Thermochemical H_2 and CO Production. *Energy Environ. Sci.* **2013**, *6*, 2424-2428.
- 36 Demont, A.; Abanades, S.; Beche, E. Investigation of Perovskite Structures as Oxygen-Exchange Redox Materials for Hydrogen Production from Thermochemical Two-Step Water-Splitting Cycles. *J. Phys. Chem. C* **2014**, *118*, 12682-12692.
- 37 Gautam, G. S.; Stechel, E. B.; Carter, E. A. Exploring Ca-Ce-M-O (M = 3d Transition Metal) Oxide Perovskites for Solar Thermochemical Applications. *Chem. Mater.* **2020**, *32*, 9964-9982.
- 38 Goldschmidt, V. M. Die Gesetze der Krystallochemie. *Naturwissenschaften* **1926**, *14*, 477–485.

- 39 Cussen, E. J.; Battle, P. D. Crystal and Magnetic Structures of 2H BaMnO₃, *Chem. Mater.* **2000**, 12, 831-838.
- 40 Macias, M. A.; Mentre, O.; Pirovano, C.; Roussel, P.; Colis, S.; Gauthier, G. H. Influence of the Synthesis Route on the Formation of 12R/10H-Polytypes and their Magnetic Properties within the Ba(Ce,Mn)O₃ Family. *New J. Chem.* **2015**, 39, 829-835.
- 41 Aich, P.; Meneghini, C.; Tortora, L.; Siruguri, V.; Kaushik, S. D.; Fu, D.; Ray, S. Fluorinated Hexagonal 4H SrMnO₃: A Locally Disordered Manganite. *J. Mater. Chem. C*, **2019**, 7, 3560-3568.
- 42 Hashimoto, S.; Iwahara, H. Structural, Thermal and Electrical Properties of Ce-doped SrMnO₃. *J. Electroceramics* **2000**, 4, 225-231.
- 43 Garten, L. M.; Selvarasu, P.; Perkins, J.; Ginley, D.; Zakutayev, A. Phase Formation of Manganese Oxide Thin Films Using Pulsed Laser Deposition. *Mater. Adv.* **2021**, 2, 303-309.
- 44 Shannon, R. D. Revised Effective Ionic Radii and Systematic Studies of Interatomic Distances in Halides and Chalcogenides. *Acta Cryst.* **1976**, A32, 751-767.
- 45 Sondena, R.; Stolen, S.; Ravindran, P.; Grande, T.; Allan, N. L. Corner-Versus Face-Sharing Octahedra in AMnO₃ Perovskites (A = Ca, Sr, and Ba). *Phys. Rev. B* **2007**, 75, 184105.
- 46 Battle, P. D.; Gibb, T. C.; Jones, C. W. The Structural and Magnetic Properties of SrMnO₃: A Reinvestigation. *J. Solid State Chem.* **1988**, 74, 60-66.

47 Jeong, C.; Ryu, J.; Noh, T.; Kim, Y. -N.; Lee, H. Structural Analysis and Electrode Performance of Ce doped SrMnO₃ Synthesised by EDTA Citrate Complexing Process. *Adv. Appl. Ceram.* **2013**, 112, 494-498.

48 Mitrovic, S.; Soedarmadji, E.; Newhouse, P. F.; Suram, S. K.; Haber, J. A.; Jin, J.; Gregoire, J. M. Colorimetric Screening for High-Throughput Discovery of Light Absorbers. *ACS Comb. Sci.* **2015**, 17, 176-181.

49 Gonzalez-Jimenez, I. N.; Climent, E.; Torres-Pardo, A.; Hernando, M.; Sanchez-Pelaez, A. E.; Fernandez-Martinez, F.; Diaz, M. T. F.; Gonzalez-Calbet, J. M.; Andres, A.; Varela, A.; Parras, M. SrMnO₃ Thermochromic Behavior Governed by Size-Dependent Structural Distortions. *Inorg. Chem.* **2016**, 55, 3980-3991.

50 Fuentes, A. F.; Boulahya, K.; Amador, U. Novel Rare-Earth-Containing Manganites Ba₄REMn₃O₁₂ (RE=Ce, Pr) with 12R structure. *J. Solid State Chem.* **2004**, 177(3), 714-720.